IEEE Access
Multidisciplinary | Rapid Review | Open Access Journal

Received December 19, 2019, accepted December 30, 2019, date of publication January 6, 2020, date of current version January 15, 2020.

Digital Object Identifier 10.1109/ACCESS.2020.2964105

Control Strategy for an Open-End Winding Induction Motor Drive System for Dual-Power Electric Vehicles

YI-FAN JIA[1], NAN XU[1], (Member, IEEE), LIANG CHU[1], YUANJIAN ZHANG[2], (Member, IEEE), ZHE XU[3], YU-KUAN LI[1], AND ZHI-HUA YANG[1]

[1]State Key Laboratory of Automotive Simulation and Control, Jilin University, Changchun 130022, China
[2]Department of Mechanical and Manufacturing Engineering, Queen's University Belfast, Belfast BT9 5BS, U.K.
[3]Research and Development Center, China FAW Group Corporation, Changchun 130011, China

Corresponding author: Nan Xu (nanxu@jlu.edu.cn)

This work was supported in part by the National Natural Science Foundation of China under Grant 51805201, and in part by the International Clean Energy Talent Program (iCET2019) of China Scholarship Council under Grant 201904100052.

ABSTRACT This work presents the control strategies for the configuration involving an open-end winding induction motor (OW-IM) fed by dual two-level inverters, which can realize the controllable power sharing between two isolated power sources without using the DC/DC converter. Based on the mathematical model of the OW-IM and the principles of the voltage vector distribution, two rotor flux calculation algorithms, namely the motor loss minimization (MLM) algorithm and the maximum power sharing capability (MPSC) algorithm are proposed and compared, with their selection strategy to select the suitable algorithm depending on the operating condition. The MLM algorithm has the optimal efficiency performance, while the MPSC algorithm can maximize the power sharing capability of the dual inverter while holding the widest operation range of the motor. Based on the dual space vector pulse-width modulation (SVPWM) control scheme, the golden section (GS) search method is introduced to allocate the stator voltage vector to the dual inverter for the power sharing demand, with a flexible iteration number to obtain a stable and efficient computational performance, which fully utilizes the power sharing capability via the voltage vector distribution. Simulation results prove the validity and the advantages of the proposed strategy. This system also lays a foundation for energy management function of the dual-power electric vehicles.

INDEX TERMS Dual-power electric vehicle, open-end winding, induction motor, dual inverter, voltage vector distribution, golden section, power sharing.

NOMENCLATURE

p_0	Number of pole-pairs
J_m	Rotational inertia of the rotor
B, C	Damping ratio and Coulomb friction torque of the rotor
R_s, R_r	Armature resistance of stator and rotor
R_c	Equivalent iron loss resistance
$L_{s\sigma}$, $L_{r\sigma}$	Leakage inductance of stator and rotor
L_m	Mutual inductance of stator and rotor
$\vec{\psi}_r$	Rotor flux vector
ω_s	Synchronous angular velocity
ω_r	Rotor angular velocity
T_e, T_l	Electromagnetic torque and load torque
$\vec{i}_s$, $\vec{i}_r$	Stator and rotor current vectors of OW-IM
i_M, i_T	Components of stator current vector in M-axis and T-axis
i_m, i_t	Components of rotor current vector in M-axis and T-axis
$\vec{i}_g$, $\vec{i}_c$	Airgap and iron loss current vectors
i_{gM}, i_{gT}	Components of airgap current vector in M-axis and T-axis
i_{cM}, i_{cT}	Components of iron loss current vector in M-axis and T-axis
$\vec{u}_s$, $\vec{u}_r$	Stator and rotor voltage vectors of the OW-IM
$\vec{u}_{s1}$, $\vec{u}_{s2}$	Output voltage vector of inverter1 and inverter2

The associate editor coordinating the review of this manuscript and approving it for publication was Xiaodong Sun.

V_{dc1}, V_{dc2}	DC-bus voltage of power source1 and power source2
u_{Am}, u_{Bm}, u_{Cm}	Inverter1's phase voltages
u_{Xn}, u_{Yn}, u_{Zn}	Inverter2's phase voltages
u_{AX}, u_{BY}, u_{CZ}	Phase voltages of the OW-IM
u_{mn}	Mid-point voltage difference between the two power sources
i_{AX}, i_{BX}, i_{CX}	Phase currents of the OW-IM
$u_{s\max}$	Maximum allowable amplitude of the stator voltage vector
$i_{s\max}$	Maximum allowable amplitude of the stator current vector
P_{inv1}, P_{inv2}	Output power of inverter1 and inverter2
P_m	Input power of the OW-IM
D_n	Inverter1's output power deviation

I. INTRODUCTION

Electric vehicles (EVs) driven by electric motors are gaining popularity in recent years and regarded as the ideal substitute for internal combustion engine vehicles (ICEVs). The permanent magnet synchronous motors (PMSMs) and the induction motors (IMs) are the two most common types of the drive motor for EVs [1]–[4]. The switched reluctance motors (SRMs) also get growing attention by their low manufacturing cost, high reliability, etc. [5]–[7] Compared with PMSM, the advantages of IM include better high-speed performance due to the less difficulty of flux-weakening operation, no rotor-position sensor, strong robustness, low cost, etc. [4], [8], [9] It is necessary to locate the rotor position of the PMSM in the vector control, thus the additional rotor-position sensor is required, otherwise the sensorless control scheme has to be implemented, which increases the system complexity [10], [11]. Moreover, the inadequate driving range of battery electric vehicles (BEVs) has spawned the electric vehicles equipped with two power sources powering the motor together, which are thus called range-extended electric vehicles (REEVs) [12]. The additional power source can be an oil-electric engine, a fuel cell, a super capacitor, etc. The traditional REEVs usually employ a DC/DC converter to maintain the DC-bus voltage, concurrently regulating the power flow between two power sources. However, the adoption of the DC/DC converter increases system complexity and cost, also brings extra power consumption [13], [14].

The configuration involving an open-end winding induction motor (OW-IM) fed by dual two-level inverters, shown in Fig. 1, has become a competitive alternative. Each end of the stator winding is fed by an independent inverter leg, which offers several advantages over the traditional single inverter configuration: 1) the motor can gain a higher phase voltage via the second inverter, resulting in a larger operating range; 2) the dual inverter can provide more phase voltage levels, enabling higher accuracy in current regulation, hence less ripple of electromagnetic torque; 3) the system has a higher reliability with the capability of operating under faulted conditions; 4) the power sharing or power flow is via the motor itself, which eliminates the additional losses from

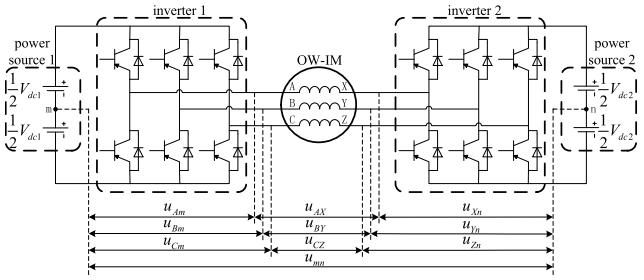

FIGURE 1. Configuration and voltage schematic of dual two-level inverter OW-IM drive system.

the DC/DC converter [15]–[20]. The main drawbacks of this configuration include the extra inverter losses caused by the additional inverter, and the inherent limitation of the power sharing range, which can be ameliorated by applying specific algorithms.

To employ the OW-IM system to EV, there are some improvements need to be made. Firstly, the operation range especially the high-speed region should be sufficient for the vehicle power performance. Secondly, the system efficiency should be high enough for the vehicle economy. Thirdly, the power sharing range between the two power sources in various operating conditions should be optimized. These improvements should be made to the torque and flux regulation layer, and the voltage modulation layer, respectively.

In the torque and flux regulation layer, the classical way is setting the rotor flux reference constant in low-speed region and inversely proportional to the rotor speed in flux-weakening region. However, by this method the motor cannot yield the maximum torque in the flux-weakening region as well as the optimal motor efficiency [21], [22]. Based on the voltage control strategy, Sang-Hoon Kim *et al.* [23] proposed a flux-weakening algorithm, which could ensure the maximum torque operation over the flux-weakening region without using the machine parameters. Based on the optimal control problem (OCP), Riadh Abdelati *et al.* [24] presented a new design of loss-minimization optimization control including a closed-loop optimal control law and the Pontryagin principle to get optimal energy consumption. Aiming at the OW-IM drive system, Ian J. Smith *et al.* [25] raised a constant power factor control method to maintain high motor power conversion efficiencies over a wide range of load settings while also providing voltage boosting for improved motor performance in high-speed region, by operating the machine with a constant fundamental power factor. Although these methods mentioned above improved the power performance and the efficiency of the motor, they did not take the power sharing into consideration. In order to fully utilize the power sharing capability between the two inverters, the torque and flux regulation method should be improved accordingly.

In the voltage modulation layer, there are plenty of researches focused on the cooperative control of the two inverters [26]–[28]. The main control target is to lower the inverter switching frequency as much as possible while

synthesizing the motor's stator voltage vector precisely. Arbind Kumar *et al.* and V.T.Somasekhar *et al.* [29], [30] proposed two strategies respectively with a similar idea of clamping one inverter to a basic voltage vector for one switching cycle while the other one was compensating the rest, which lowered the device switching frequency of the dual inverter so as to reduce inverter losses. Kodumur Meesala Ravi Eswar *et al.* [31] proposed an improved predictive torque and flux control scheme, whose nearest voltage vector selection strategy reduced the number of prediction voltage vectors in each sample interval and thus reduced the flux ripple, device switching frequency and the calculation complexity. There are also researches paying attention to the power sharing between the two inverters. In order to achieve the controllable power sharing, Domenico Casadei *et al.* [32] studied the multilevel operation of the dual inverter. By using different vector combinations in specific voltage vector regions, the proposed method could regulate the power sharing of dual inverter in a limited range while synthesizing the expected voltage vector in a relative low switching frequency. Liang Chu *et al.* [33] proposed a multi-level current hysteresis modulation scheme by using the dual inverter as a four-level operator that could achieve two power sharing levels.

Instead of the cooperative control of the dual inverter, controlling two inverters separately gives another way to achieve the power sharing function, which is the voltage vector distribution. The voltage vector distribution works when the two inverters are both under space vector pulse-width modulation (SVPWM), namely the dual SVPWM control scheme. Based on this scheme, Brian A. Welchko [34] proposed three strategies to achieve different power sharing effects, which could maximize the output power of the primary power source, the available voltage margin for dynamic performance, and the input power of the motor accordingly. Based on the battery-capacitor configuration, Albino Amerise *et al.* [35] developed a robust rotor-field oriented control system, which adapted the voltage of the floating capacitor to the actual operating condition and reduced the switching losses. This control scheme improved the efficiency in the region around the base speed and at high torque values. In our previous work [36], based on the dual SVPWM control scheme, four voltage vector distribution patterns were proposed, with their selection strategy selecting the optimal solution according to the operating conditions. By using specific basic voltage vectors and saturated voltage vectors, the power sharing demand could be achieved while the inverter switching frequency was lowered. However, this strategy had a considerable computational complexity, so that it was difficult to apply in practical application.

Towards this issue, the present paper attempts to propose a torque and flux regulation algorithm, which can combine and balance the demand of the system efficiency and the power sharing capability. Also a voltage vector distribution method is proposed to support the power sharing function with a relatively light computational burden. This paper is organized as follow. In Section II, after presenting the overall configuration of the system, the mathematical model of the OW-IM, the principles of the dual inverter's voltage vector distribution and the power sharing are introduced. Section III works on the torque and flux regulation. Two flux calculation algorithms are proposed, aiming to optimize the system efficiency and the power sharing capability, respectively. To realize the power sharing operation, Section IV introduces a voltage vector distribution method based on the golden section algorithm with a preset iteration number. In Section V, a detailed simulation is executed to verify the proposed control scheme.

II. MATHEMATICAL MODELS OF MOTOR AND VOLTAGE VECTOR DISTRIBUTION

After introducing the overall configuration of the proposed system, this section deals with the mathematical model of the OW-IM based on the equivalent circuits in the synchronous rotating frame. To quantitatively analyze the motor loss and efficiency, the copper loss as well as the iron loss is taken into account. The principles of the dual inverter's voltage vector distribution and power sharing are discussed with respective to the motor's stator plane. In particular, in order to highlight the power flow, the Clarke and Park transformations among different reference frames in this paper are in equal power form instead of equal amplitude form, thus the coefficient of the transformation matrix is $\sqrt{2/3}$ instead of $2/3$.

A. SYSTEM OVERALL CONFIGURATION

As shown in Fig. 2, the drive system is composed of the drive system circuit and its controller. In the circuit part, the OW-IM is fed by two two-level inverters powered by two isolated power sources. Two capacitors are employed in parallel with the power sources in order to provide necessary reactive power and filter the voltage fluctuation.

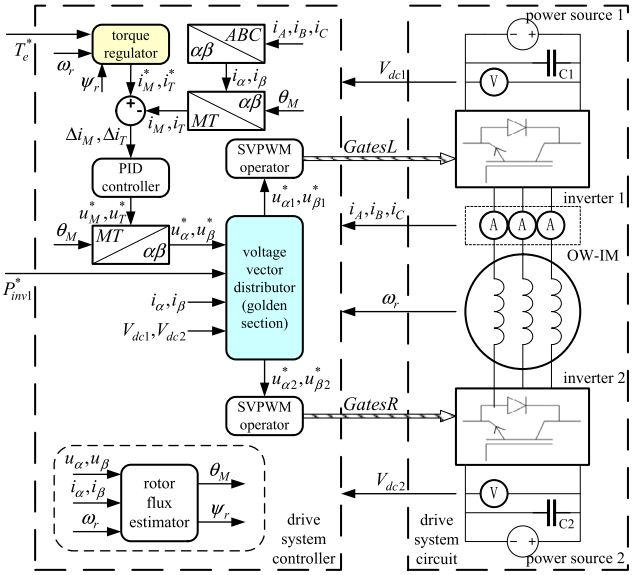

FIGURE 2. Overall configuration of the OW-IM drive system.

The system controller receives the expected torque T_e^* and the desired output power of inverter1 P_{inv1}^* from the vehicle

control unit (VCU), and delivers the gate control signals *GatesL* and *GatesR* to inverter1 and inverter2, respectively. Specifically, the rotor flux estimator outputs the angle of the rotor field θ_M in the stationary reference frame, thus the transformation between the stationary reference frame ($\alpha\beta$ frame) and the synchronous rotating reference frame (MT frame) can be implemented. In the torque regulator, the desired stator current $\vec{i}_s^*$ is calculated to generate the corresponding electromagnetic torque. Then a PID controller is engaged to provide the desired stator voltage vector $\vec{u}_{s1}^*$ using the stator current error $\Delta\vec{i}_s$. After being transformed to $\alpha\beta$ frame, in the voltage vector distributor, $\vec{u}_s^*$ is divided into $\vec{u}_{s1}^*$ and $\vec{u}_{s2}^*$, which are the desired voltage vectors of inverter1 and inverter2, respectively, to the corresponding SVPWM operators. This paper mainly focuses on the torque regulator marked in yellow and the voltage vector distributor marked in blue.

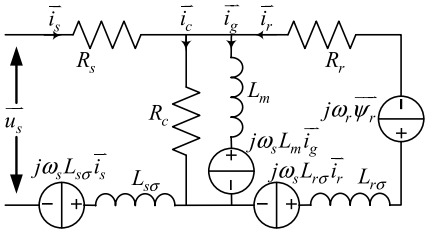

FIGURE 3. Dynamic equivalent circuit of the OW-IM in MT frame.

B. MATHEMATICAL MODEL OF THE OW-IM

The dynamic equivalent circuit of the OW-IM in the synchronous rotating reference frame is shown in Fig. 3. We give the equivalent circuit in the vector form instead of the coordinate components. Where R_s and R_r are the armature resistance of the stator and the rotor, R_c is the equivalent iron loss resistance. $L_{s\sigma}$, $L_{r\sigma}$ are the leakage inductance of the stator and the rotor, L_m is the mutual inductance. ω_s and ω_r are the synchronous angular velocity and the rotor angular velocity, respectively. $\vec{u}_s$ is the stator voltage vector. $\vec{i}_s$, $\vec{i}_r$, $\vec{i}_g$ and $\vec{i}_c$ are the current vectors of the stator, the rotor, the airgap, and the equivalent iron loss resistance, respectively. $\underset{\psi_r}{\rightharpoonup}$ is the rotor flux vector, and we have $\underset{\psi_r}{\rightharpoonup} = L_{r\sigma}\vec{i}_r + L_m\vec{i}_g$. Except for the motional electromotive force (EMF) $j\omega_r\vec{\psi}_r$, the EMFs in series with the inductance are the inductive EMF caused by the rotating MT frame.

Therefore, in MT frame, the mathematical model of the OW-IM is described as follow, also in the vector form:

$$\begin{cases} \vec{u}_s = R_s\vec{i}_s + p(L_{s\sigma}\vec{i}_s + L_m\vec{i}_g) + j\omega_s(L_{s\sigma}\vec{i}_s + L_m\vec{i}_g) \\ \vec{u}_r = R_r\vec{i}_r + p(L_{r\sigma}\vec{i}_r + L_m\vec{i}_g) + j\omega_f(L_{r\sigma}\vec{i}_r + L_m\vec{i}_g) \\ 0 = R_c\vec{i}_c - pL_m\vec{i}_g - j\omega_s L_m\vec{i}_g \end{cases} \tag{1}$$

The three equations are the voltage equations of the stator circuit, the rotor circuit and the airgap circuit, respectively. Where p is the differential operator and ω_f is the slip angular velocity, and we have $\omega_f = \omega_s - \omega_r$. Because the OW-IM we use is squirrel-cage type, $\vec{u}_r = 0$ is satisfied. The relation between the current vectors is shown by (2):

$$\vec{i}_s + \vec{i}_r = \vec{i}_g + \vec{i}_c \tag{2}$$

Because in MT frame the Axis-M is collinear with $\underset{\psi_r}{\rightharpoonup}$, the electromagnetic torque T_e generated by the motor can be described by the following equation in a simple form:

$$T_e = -p_0\psi_r i_t \tag{3}$$

where p_0 is the number of pole-pairs, and i_t is the component of the rotor current vector $\vec{i}_r$ in T-axis.

The kinematical equation of the rotor can be described as:

$$pJ_m\omega_m = T_e - (T_l + B\omega_m + C) \tag{4}$$

where T_l is the load torque, ω_m is the rotor's mechanical angular velocity, and J_m is the rotational inertia of the rotor. B is the damping ratio and C is the Coulomb friction torque.

Then the efficiency of the OW-IM can be described as:

$$\begin{cases} \eta_{mot} = T_l\omega_m/(\vec{u}_s\cdot\vec{i}_s) \\ \eta_{gen} = (\vec{u}_s\cdot\vec{i}_s)/T_l\omega_m \end{cases} \tag{5}$$

where η_{mot} is the efficiency when the motor is in motoring condition and η_{gen} is that in generating condition.

C. PRINCIPLES OF THE DUAL INVERTER'S VOLTAGE VECTOR DISTRIBUTION AND POWER SHARING

To facilitate the derivation, two virtual points m and n are introduced to split the voltages of the power sources V_{dc1} and V_{dc2} in halves, as shown in Fig. 1. Thus, the voltage vectors generated by the two inverters can be obtained as:

$$\begin{cases} \vec{u}_{s1} = \sqrt{2/3}(u_{Am}e^{j0} + u_{Bm}e^{j2\pi/3} + u_{Cm}e^{j4\pi/3}) \\ \vec{u}_{s2} = \sqrt{2/3}(u_{Xn}e^{j0} + u_{Yn}e^{j2\pi/3} + u_{Zn}e^{j4\pi/3}) \end{cases} \tag{6}$$

As shown in Fig. 1, u_{Am}, u_{Bm} and u_{Cm} are the phase voltages of inverter1, u_{Xn}, u_{Yn} and u_{Zn} are the phase voltages of inverter2. $\vec{u}_{s1}$ and $\vec{u}_{s2}$ are the voltage vectors generated by inverter1 and inverter2, respectively. In the expressions, e^{j0}, $e^{j2\pi/3}$ and $e^{j4\pi/3}$ are the spatial operators indicating the orientations of the three motor's phases.

Also, the stator voltage vector of the OW-IM, denoted as $\vec{u}_s$, can be synthesized by the motor's phase voltages u_{AX}, u_{BY} and u_{CZ} in the same way:

$$\vec{u}_s = \sqrt{2/3}(u_{AX}e^{j0} + u_{BY}e^{j2\pi/3} + u_{CZ}e^{j4\pi/3}) \tag{7}$$

We can also acquire the following relations in phase voltages by Fig. 1:

$$\begin{cases} u_{AX} = u_{Am} - u_{Xn} + u_{mn} \\ u_{BY} = u_{Bm} - u_{Yn} + u_{mn} \\ u_{CZ} = u_{Cm} - u_{Zn} + u_{mn} \end{cases} \tag{8}$$

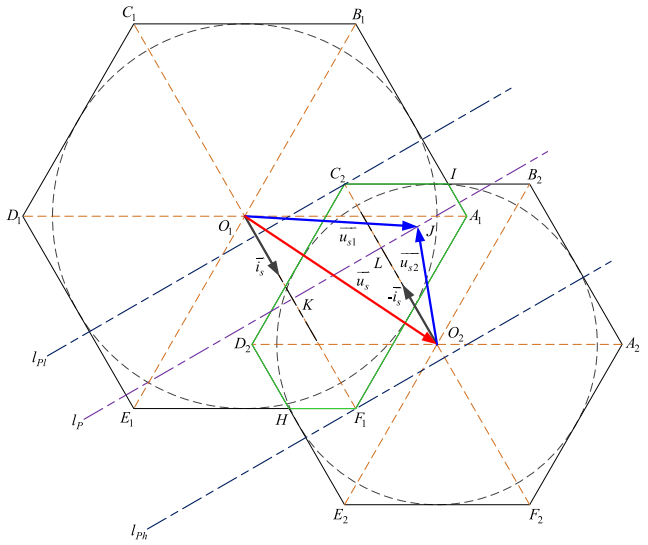

FIGURE 4. Schematic diagram of the dual inverter voltage vector distribution.

where u_{mn} is the voltage difference between the two power sources' midpoints m and n.

By substituting (6) and (8) into (7), the relation among the voltage vectors in the motor's stator plane can be derived as:

$$\vec{u_s}=\vec{u_{s1}}-\vec{u_{s2}}+\sqrt{2/3}u_{mn}(e^{j0}+e^{j2\pi/3}+e^{j4\pi/3})=-\vec{u_{s1}}-\vec{u_{s2}} \tag{9}$$

From (9) it can be observed that $\vec{u_s}$ can be easily obtained by subtracting $\vec{u_{s2}}$ from $\vec{u_{s1}}$ without involving the floating midpoint voltage difference u_{mn}. In essence, u_{mn} leaves an identical effect on u_{AX}, u_{BY} and u_{CZ} so that they counteract each other when synthesizing and finally leave no effect on $\vec{u_s}$. In other words, u_{mn} acts as a zero-sequence component independent of the motor's stator plane.

The phase stator currents of the motor i_{AX}, i_{BX} and i_{CX} are measured by the current sensors, then the stator current vector $\vec{i_s}$, can be synthesized as:

$$\vec{i_s}=\sqrt{2/3}(i_{AX}e^{j0}+i_{BY}e^{j2\pi/3}+i_{CZ}e^{j4\pi/3}) \tag{10}$$

After $\vec{i_s}$ and the expected $\vec{u_s}$ are obtained, the voltage vector distribution and the power sharing between the two inverters can be studied. As shown in Fig. 4, in the stationary $\alpha\beta$ frame, the red vector $\vec{u_s}$ is synthesized by the blue vectors $\vec{u_{s1}}$ and $\vec{u_{s2}}$, which satisfies the relation expressed in (9). Point O_1 and O_2 are the start points of vectors $\vec{u_{s1}}$ and $\vec{u_{s2}}$, which indicate the centers of the modulation ranges of inverter1 and inverter2. Thus, the hexagon $A_1B_1C_1D_1E_1F_1$ with a radius of $\sqrt{2/3}V_{dc1}$ indicates inverter1's modulation range under SVPWM, and the hexagon $A_2B_2C_2D_2E_2F_2$ with a radius of $\sqrt{2/3}V_{dc2}$ indicates inverter2's. The overlapping area of the two hexagons $A_1IC_2D_2HF_1$ with the green boundary provides the feasible region of the common end point of $\vec{u_{s1}}$ and $\vec{u_{s2}}$, which is also the feasible region of the voltage vector distribution. In other words, the essence of the voltage vector distribution is to determine the location of the common end of $\vec{u_{s1}}$ and $\vec{u_{s2}}$, marked as point J, within the range of $A_1IC_2D_2HF_1$.

Because the defined directions of phase stator currents are from inverter1 to inverter2, as shown in Fig. 1, the stator current vector observed from inverter2 is opposite to that from inverter1. Thus, the input power of the motor, denoted as P_m, and the output power of inverter1 and inverter2, denoted as P_{inv1} and P_{inv2}, can be acquired as:

$$\begin{cases} P_m = \vec{u_s}\cdot\vec{i_s} \\ P_{inv1} = \vec{u_{s1}}\cdot\vec{i_s} \\ P_{inv2} = \vec{u_{s2}}\cdot(-\vec{i_s}) = -\vec{u_{s2}}\cdot\vec{i_s} \end{cases} \tag{11}$$

In Fig. 4, P_{inv1} and P_{inv2} can be obtained by the scalar product of $\vec{u_{s1}}$ and $\vec{i_s}$ at point O_1, as well as $\vec{u_{s2}}$ and $-\vec{i_s}$ at point O_2. Line l_P is perpendicular to $\vec{i_s}$ and going through point J, which gives a track of the voltage vector distribution points where the power sharing between the two inverters holds constant. In other words, all the points on line l_P obtain the same P_{inv1} and P_{inv2}. By moving line l_P along with the direction of $\vec{i_s}$ while keeping it not leaving polygon $A_1IC_2D_2HF_1$, the feasible region of power sharing can be acquired, with two boundary lines l_{Pl} and l_{Ph}, representing the minimum and the maximum output power of inverter1.

It is worth mentioning that the discussion above is based on the stationary $\alpha\beta$ frame. If we want to analyze the motor's operating point in steady state, $\vec{u_s}$ and $\vec{i_s}$ are given in the synchronous rotating frame. Under this circumstance, the amplitudes of $\vec{u_s}$ and $\vec{i_s}$, as well as the angle between them remain unchanged, but the modulation ranges of the two inverters are revolving on their centers as θ_M varies. Thus, the two hexagons should be replaced with their inscribed circles to represent the modulation ranges in synchronous rotating frame, at the same time the feasible region of the voltage vector distribution shrinks to the overlapping area of the two circles, shown in Fig. 4. The radiuses of the two circles are $\sqrt{1/2}V_{dc1}$ and $\sqrt{1/2}V_{dc2}$, respectively.

III. TORQUE AND FLUX REGULATION STRATEGY

This section deals with the torque and flux regulation strategy. Two flux calculation algorithms are proposed and compared, aiming to optimize the motor efficiency and the power sharing capability, respectively. The proper algorithm will be selected depending on the operating condition.

A. MOTOR LOSS MINIMIZATION ALGORITHM

The controllable motor loss can be divided into the copper loss and the iron loss. They also contribute to most of the electrical loss of the motor. Motor loss minimization (MLM) algorithm aims to minimize the copper loss and the iron loss in steady state of the motor's operation.

In steady state, the rotor flux amplitude ψ_r holds constant, thus the rotor currents can be described as:

$$\begin{cases} i_m = 0 \\ i_t = -T_e/p_0\psi_r \end{cases} \tag{12}$$

The copper loss can be obtained as:

$$P_{Cu} = R_s|\vec{i_s}|^2 + R_r|\vec{i_r}|^2 = R_s(i_M^2 + i_T^2) + R_r(i_m^2 + i_t^2) \tag{13}$$

where i_M and i_T are the components of $\vec{i_s}$, i_m and i_t are the components of $\vec{i_r}$ in M-axis and T-axis.

The iron loss can be obtained as:

$$P_{Fe} = R_c|\vec{i_c}|^2 = R_c(i_{cM}^2 + i_{cT}^2) \tag{14}$$

where i_{cM} and i_{cT} are the components of $\vec{i_c}$ in M-axis and T-axis.

In steady state, the leakage inductance of the motor, namely $L_{s\sigma}$ and $L_{r\sigma}$, barely affect the electrical loss of the motor due to their ultra-low value compared with L_m, so that they are ignored for convenience. Thus, the components of the airgap current vector $\vec{i_g}$ in M-axis and T-axis can be easily acquired as:

$$\begin{cases} i_{gM} = \psi_r/L_m \\ i_{gT} = 0 \end{cases} \tag{15}$$

From Fig. 3 we can also obtain the iron loss current by Kirchhoff's voltage law:

$$\begin{cases} i_{cM} = -\omega_s L_m i_{gT}/R_c \\ i_{cT} = \omega_s L_m i_{gM}/R_c \end{cases} \tag{16}$$

Afterwards, by simultaneous equations (12)-(16), the partial derivative of the copper and iron loss to the rotor flux linkage can be calculated as:

$$\begin{aligned} &\partial(P_{Cu} + P_{Fe})/\partial\psi_r \\ &= 2\{p_0^2[R_s R_c^2 + \omega_r^2 L_m^2(R_s + R_c)]\psi_r^4 \\ &\quad -T_e^2 L_m^2[R_s(R_s + R_c)^2 + R_r R_c(R_r + R_c)]\}/p_0^2 R_c^2 L_m^2 \psi_r^3 \end{aligned} \tag{17}$$

By making $\partial(P_{Cu} + P_{Fe})/\partial\psi_r = 0$ we can acquire the extreme point of $P_{Cu} + P_{Fe}$. Because the denominator and the quartic coefficient of $\partial(P_{Cu} + P_{Fe})/\partial\psi_r = 0$ are positive, the solution on the right side is where the function curve crosses the abscissa axis from below to above, thus is the minimum point of $P_{Cu} + P_{Fe}$ we want. Either there is no valid solution of the above equation, or the amplitude of $\vec{u_s}$ or $\vec{i_s}$ corresponding to the solution exceeds their upper limits, it means the present operating point is out of the motor's operating range. By obtaining the ψ_r value corresponding to the minimum $P_{Cu} + P_{Fe}$ at each valid operating point of the motor, we can obtain the look-up table of ψ_r in the motor's operating range of the loss minimization strategy.

B. MAXIMUM POWER SHARING CAPABILITY ALGORITHM

From Section II(C) we know the power sharing capability of the dual inverter is mainly up to the size of the feasible region of the voltage vector distribution, which is the overlapping area of the two inverters' voltage modulation range. If $\vec{u_s}$ is linearly distributed to the dual inverter, which means $\vec{u_{s1}}$ and $\vec{u_{s2}}$ are collinear with $\vec{u_s}$, the power sharing ratio of dual inverter is exactly the voltage vector amplitude ratio, shown as follow:

$$P_{inv1} : P_{inv2} : P_m = |\vec{u_{s1}}| : |\vec{u_{s2}}| : |\vec{u_s}| \tag{18}$$

When V_{dc1} and V_{dc2} are determined, the size of this feasible region only depends on the amplitude of $\vec{u_s}$. Therefore, the maximum power sharing capability (MPSC) algorithm aims to minimize the amplitude of the stator voltage vector $\vec{u_s}$ in steady state of the motor's operation.

First, we need to derive the unconstrained expression of the minimum $|\vec{u_s}|$. From Fig. 3 the airgap current can be obtained as:

$$\begin{cases} i_{gM} = (\psi_r - L_{r\sigma} i_m)/L_m \\ i_{gT} = -L_{r\sigma} i_t/L_m \end{cases} \tag{19}$$

This time we take the leakage inductances into consideration but to neglect the iron loss current $\vec{i_c}$. Because the equivalent iron loss resistance R_c is in parallel with the stator circuit as well as the rotor circuit, the current through it barely influence the stator voltage $\vec{u_s}$.

Therefore, expression (2) becomes $\vec{i_s} + \vec{i_r} = \vec{i_g}$. By substituting (12) and (19) into (1), the square of $|\vec{u_s}|$ can be calculated as:

$$\begin{aligned} u_s^2 = &\{\psi_r R_s/L_m - T_e(p_0\psi_r^2\omega_r + T_e R_r)[L_m(L_{s\sigma} + L_{r\sigma}) \\ &+ L_{s\sigma}L_{r\sigma}]/p_0^2 L_m \psi_r^3\}^2 \\ &+ T_e[L_m(R_s + R_r) + R_s L_{r\sigma} + R_r L_{s\sigma}] \\ &+ p_0\psi_r^2\omega_r L_s/p_0^2 L_m^2\psi_r^2 \end{aligned} \tag{20}$$

Afterwards, the partial derivative of u_s^2 to ψ_r can be calculated as:

$$\partial u_s^2/\partial\psi_r = f_{MVVA}/k_{MVVA} \tag{21}$$

where f_{MVVA} is the minimum voltage vector amplitude equation, and can be described as:

$$\begin{aligned} f_{MVVA} = &p_0^4(R_s^2 + L_s^2\omega_r^2)\psi_r^8 \\ &- p_0^2 T_e^2[\omega_r^2(L_s L_r - L_m^2)^2 + (R_s L_r + R_r L_s)^2 \\ &- 2R_s R_r(L_s L_r - L_m^2)]\psi_r^4 \\ &- 4p_0\omega_r T_e^3 R_r(L_s L_r - L_m^2)^2\psi_r^2 - 3T_e^4 R_r^2(L_s L_r - L_m^2)^2 \end{aligned} \tag{22}$$

where we have $L_s = L_m + L_{s\sigma}$ and $L_r = L_m + L_{r\sigma}$. The denominator k_{MVVA} can be described as:

$$k_{MVVA} = p_0^4 L_m^2 \psi_r^7/2 \tag{23}$$

Similar to the loss minimization strategy, by making $\partial u_s^2/\partial \psi_r = 0$ we can acquire the extreme point of u_s^2. Because k_{MVVA} and the octant coefficient of f_{MVVA} are positive, the solution on the right side is where the function curve crosses the abscissa axis from below to above, thus is the minimum point of u_s^2 we want.

Although there is a valid solution of the minimum voltage vector amplitude equation f_{MVVA}, the operating point is limited by the voltage capacity of the power sources and the current capacity of the inverters, which means the amplitudes of $\vec{u_s}$ and $\vec{i_s}$ corresponding to the solution have to satisfy $|\vec{u_s}| \leq u_{s\max}$ and $|\vec{i_s}| \leq i_{s\max}$, where $u_{s\max}$ and $i_{s\max}$ are the maximum allowable amplitudes of $\vec{u_s}$ and $\vec{i_s}$, respectively. Therefore, if $|\vec{u_s}| > u_{s\max}$ holds, it means even the minimum $|\vec{u_s}|$ exceeds the voltage limit. In this situation the corresponding operating point cannot be reached because the voltage is saturated. But if $|\vec{u_s}| \leq u_{s\max}$ and $|\vec{i_s}| > i_{s\max}$ hold, the minimum $|\vec{u_s}|$ is restricted by the current limit. In this situation $|\vec{u_s}|$ gets its minimum amplitude when $|\vec{i_s}| = i_{s\max}$ holds duo to the function monotonicity.

This time we take both the leakage inductances and the equivalent iron loss resistance into account. By substituting (12), (16) and (19) into $i_M^2 + i_T^2 = i_{s\max}^2$, the maximum current vector amplitude equation can be acquired as:

$$\begin{aligned} f_{MCVA} = {} & p_0^4(R_c^2 + L_m^2\omega_r^2)\psi_r^8 + p_0^3 L_m^2(2\omega_r T_e(R_r + R_c) \\ & - p_0 R_c^2 i_{s\max}^2)\psi_r^6 \\ & + p_0^2 T_e^2\{L_m^2[(R_r + R_c)^2 + \omega_r^2 L_{r\sigma}^2] \\ & + R_c^2 L_{r\sigma}(2L_m + L_{r\sigma})\}\psi_r^4 \\ & + 2p_0\omega_r T_e^3 R_r L_m^2 L_{r\sigma}^2 \psi_r^2 + T_e^4 R_r^2 L_m^2 L_{r\sigma}^2 \end{aligned} \tag{24}$$

The solution with a lower $|\vec{u_s}|$ is the valid solution of equation f_{MCVA}.

In conclusion, at each operating point of the motor, the solution of equation f_{MVVA} will be tried first. If it fails, the solution of equation f_{MCVA} will be selected as the ψ_r value of the maximum power sharing capability strategy.

C. CAMPARION AND SELECTION STRATEGY OF THE ALGORITHMS

We have proposed three rotor flux calculation methods yet, which are the motor loss minimization (MLM) method, the minimum voltage vector amplitude (MVVA) method, and the maximum current vector amplitude (MCVA) method. The first method is the MLM algorithm itself, and the latter two methods form the maximum power sharing capability (MPSC) algorithm. Then we need to compare these methods and give the selection strategy.

Table 1 gives the parameters of the OW-IM we use, which is suitable for vehicle drive system. Particularly, the sum of V_{dc1} and V_{dc2} is set to 600V, thus the maximum amplitude of $\vec{u_s}$ satisfies $u_{s\max} = \sqrt{2/3} \times \sqrt{3}/2 \times 600 = \sqrt{1/2} \times 600$, in which $\sqrt{2/3}$ is the coefficient of the equal power transformation, $\sqrt{3}/2$ is the radius ratio of the inscribed circle and its circumscribed hexagon representing the voltage modulation range under SVPWM. The phase current limit is set to 260A, thus the maximum amplitude of $\vec{i_s}$ satisfies $i_{s\max} = \sqrt{2/3} \times 3/2 \times 260 = \sqrt{3/2} \times 600$, in which $3/2$ is the amplitude ratio of the synthesized $\vec{i_s}$ and the component sinusoidal phase current.

TABLE 1. Parameters of the OW-IM.

Modules	Items	Parameters
OW-IM	motor type	squirrel-cage
	number of pole pairs p_0	4
	stator armature resistance R_s/Ω	0.025
	rotor armature resistance R_r/Ω	0.035
	equivalent iron loss resistance R_c/Ω	110
	mutual inductance L_m/F	0.0012
	leakage inductance of the stator and rotor [$L_{s\sigma}$, $L_{r\sigma}$]/F	[0.00015, 0.00017]
	rotational inertia of rotor J_m /kgm^{-2}	0.045
	Cullen and viscous resistance coefficient	[0.05, 0.0001]
circuit restrictions	maximum amplitude of $\vec{u_s}$ $u_{s\max}$ /V	$\sqrt{1/2}\times 600$
	maximum amplitude of $\vec{i_s}$ $i_{s\max}$ /V	$\sqrt{3/2}\times 260$

The operation ranges of the motor are the first and the fourth quadrants. The first quadrant of the motor's operating area represents the motoring state and the fourth quadrant represents the generating state, which occurs during the regenerative braking period. The second and the third quadrants represent the opposite revolving direction, which are completely symmetric with the first and the fourth quadrants.

The rotor flux amplitude maps of the three algorithms are shown in Fig. 5, which give the expected rotor flux amplitude in each operating point of the motor.

It can be seen that by combining the MVVA and the MCVA algorithms, the motor operating range of the maximum power sharing capability algorithm is obviously larger than the motor loss minimization algorithm, which enhances the dynamic performance of the vehicle. In all the three algorithms, the rotor flux amplitude is positively correlated with the motor output torque. However, at the same operating point, the rotor flux amplitudes of the MVVA and the MCVA algorithms are significantly lower than the MLM algorithm, hence resulting in relatively lower EMFs and lower amplitudes of the stator voltage vector, which can also be observed in Fig. 6.

Fig. 6 shows the stator voltage saturability maps of the three algorithms. The higher the stator voltage saturability is, the less the voltage margin remains, resulting in less capability of power sharing. As mentioned above, due to the relatively lower rotor flux amplitudes, the MVVA and the MCVA algorithms have significantly lower voltage saturability than the MLM algorithm at the same operating point, especially in

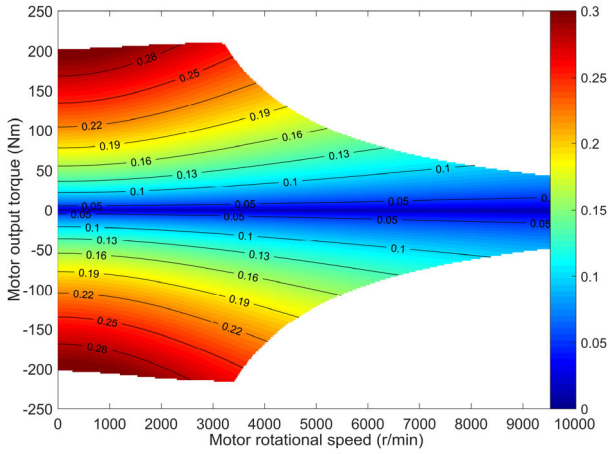

a) The MLM algorithm

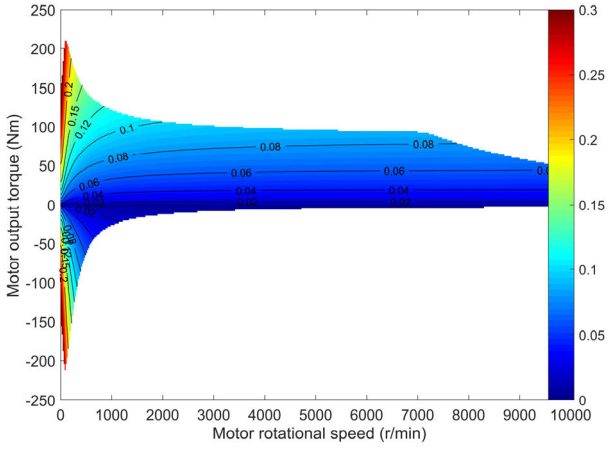

b) The MVVA algorithm

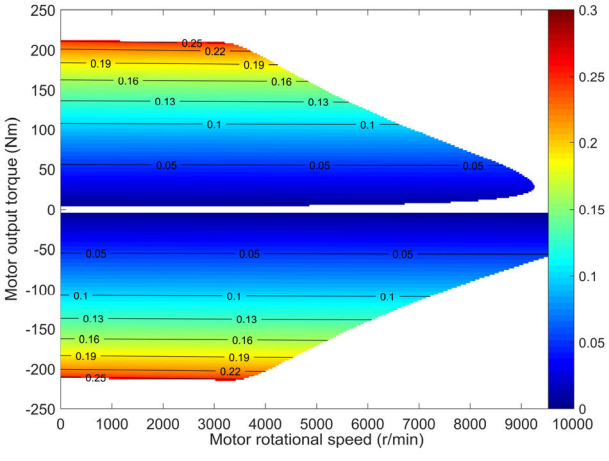

c) The MCVA algorithm

FIGURE 5. The rotor flux amplitude maps of the three algorithms.

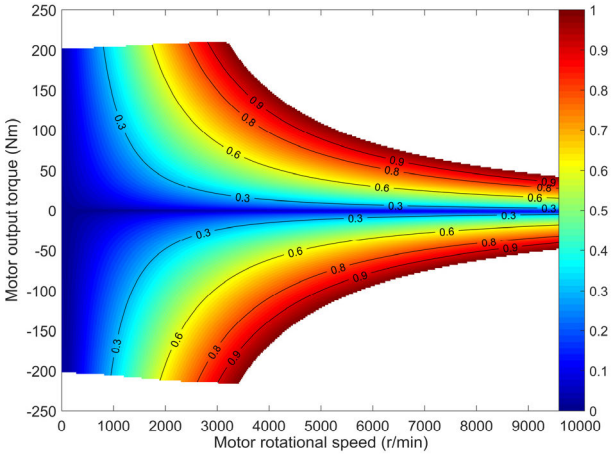

a) The MLM algorithm

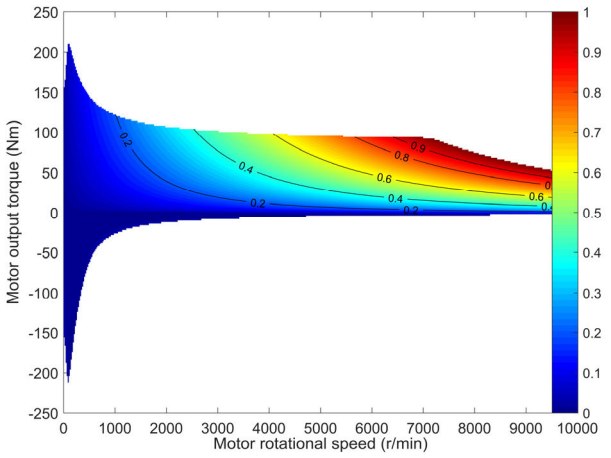

b) The MVVA algorithm

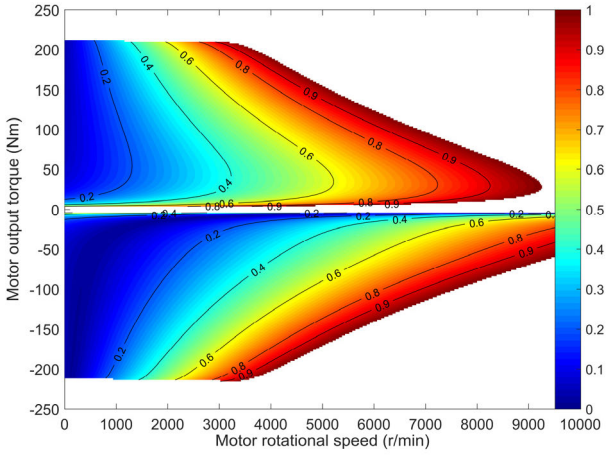

c) The MCVA algorithm

FIGURE 6. The voltage saturability maps of the three algorithms.

the low-speed area, which endows the algorithms with more power sharing capability.

Fig. 7 gives the motor efficiency characteristic of the three algorithms.

We can observe that all the three algorithms have pretty good efficiency characteristics with their maximum efficiency up to 90%. Their high-efficiency areas are all at the high-speed heavy-load area, but the size of the high-efficiency area under the MLM algorithm is significantly larger than the MVVA and the MCVA algorithms, which gives the MLM algorithm a better efficiency performance in low-speed area and light-load area.

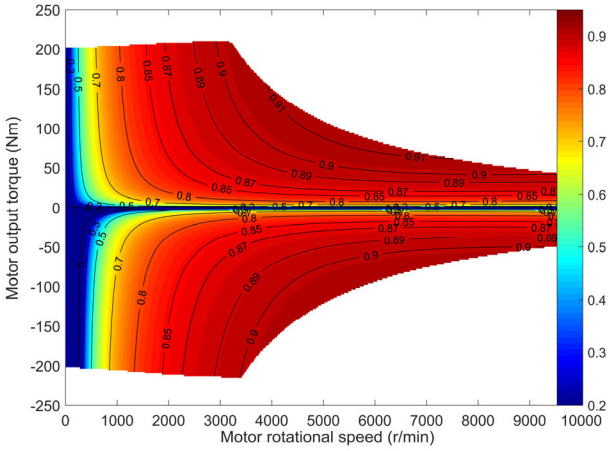

a) The MLM algorithm

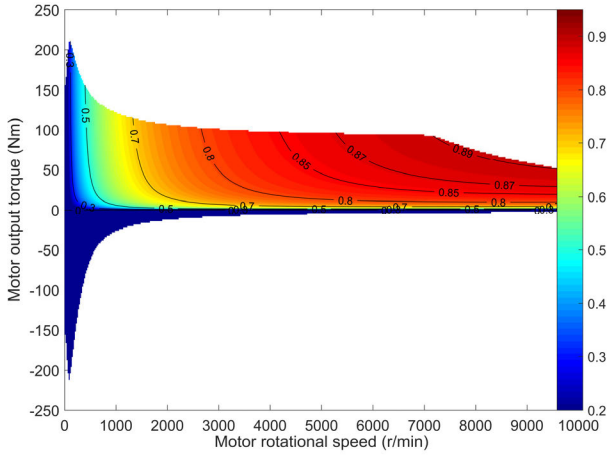

b) The MVVA algorithm

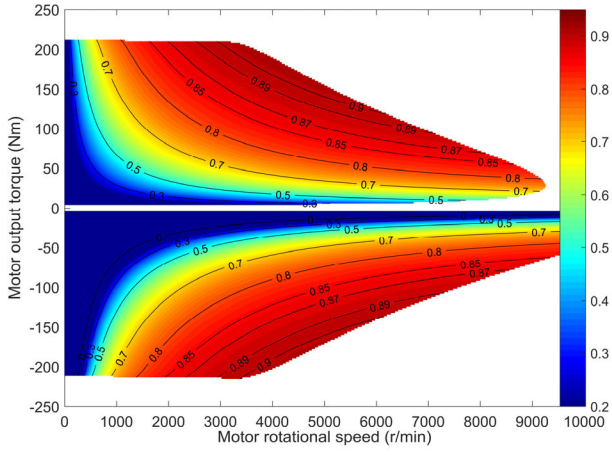

c) The MCVA algorithm

FIGURE 7. The motor efficiency maps of the three algorithms.

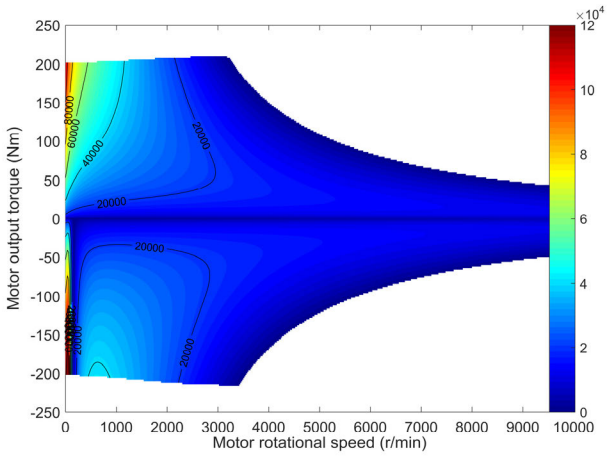

a) The MLM algorithm

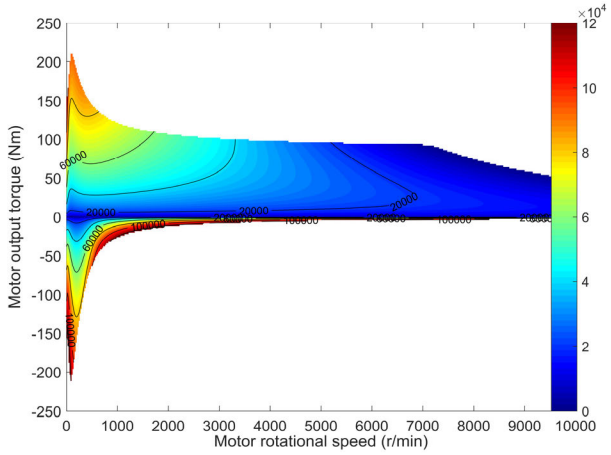

b) The MVVA algorithm

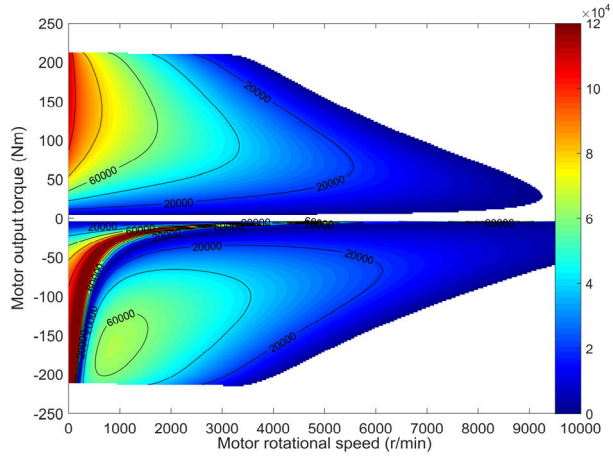

c) The MCVA algorithm

FIGURE 8. Inverter1's output power span of the three algorithms.

At a certain operating point, the difference between the maximum and the minimum attainable output power of inverter1 is defined as inverter1's output power span, representing the power sharing capability of the operating point. The maps of inverter1's output power span of the three algorithms are shown in Fig. 8.

It can be seen that the MLM algorithm barely has the power sharing capability in high-speed area. Only in low-speed heavy-load area can it distribute some power between the dual inverter. On the contrary, the power sharing ranges of the MVVA and the MCVA algorithms keep a relatively high value in most of the operating area. When the motor is

in an extremely high-speed heavy-load operating condition, there is no voltage margin left, thus all the three algorithms do not have the power sharing capability. However, the relatively low stator voltage of the MVVA and the MCVA algorithms give them higher torque limits in high-speed area.

In conclusion, the MLM algorithm has a better efficiency characteristic, but the MPSC (MVVA+MCVA) algorithm has a larger operating range and better power sharing capability. The rotor flux calculation algorithm selection strategy should follow the principles: 1) guarantee the sufficient dynamic performance; 2) attain a better efficiency based on the realization of the power sharing demand. Therefore, the MLM algorithm should be selected if the present operating point is attainable and the power sharing demand can be met by the MLM algorithm itself. Otherwise, the MPSC algorithm should be selected. In detail, the MVVA algorithm should be selected if its operating range covers the current operating point, otherwise the MCVA algorithm should be implemented. The flow chart of the rotor flux selection strategy is given in Fig. 9. Where OP is the present operating point of the motor; R_{OP_MLM}, R_{OP_MVVA}, R_{OP_MCVA} are the operating ranges of the MLM, MVVA, MCVA algorithm; ψ_{r_MLM}, ψ_{r_MVVA}, ψ_{r_MCVA} are the expected rotor flux amplitudes of the MLM, MVVA, MCVA algorithm, respectively; and R_{Pinv1_MLM} is inverter1's output power range of the MLM algorithm.

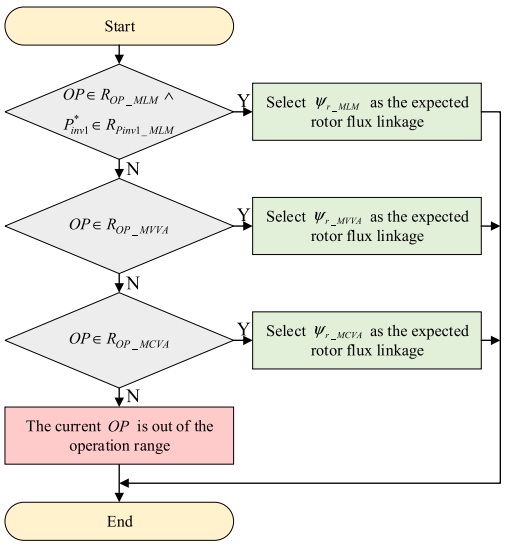

FIGURE 9. Flow chart of the rotor flux selection strategy.

IV. VOLTAGE VECTOR DISTRIBUTION STRATEGY

After the expected rotor flux amplitude ψ_r^* is given, the expected stator current can be calculated by the following equations (ignoring R_c):

$$\begin{cases} i_M^* = \psi_r^*/L_m \\ i_T^* = T_e^* L_r/(p_0 L_m \psi_r) \end{cases} \tag{25}$$

It is worth mentioning that when we shift the rotor flux calculation algorithms, there might be a saltation of the expected rotor flux ψ_r^*. However, the actual ψ_r will change gradually due to the inductance inertia. In order to ensure the accuracy of the torque control, the expected stator current of T-axis i_T^* is calculated using the actual ψ_r given by the rotor flux estimator. Add a rate limiter to ψ_r^* if necessary.

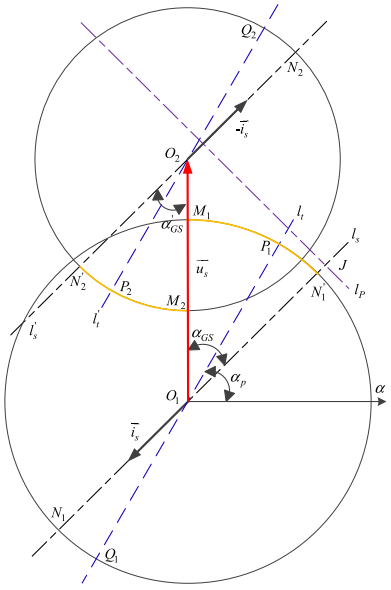

FIGURE 10. Schematic diagram of the searching boundary.

As shown in Fig. 2, a PID controller is engaged to calculate the desired stator voltage vector $\vec{u}_s^*$. Afterwards, we need to allocate $\vec{u}_s^*$ to inverter1 and inverter2 according to the power sharing demand, which is expressed by the desired output power of inverter1 P_{inv1}^*. This section deals with the voltage vector distribution strategy.

A. BASIC PRINCIPLES AND SEARCHING BOUNDARY

The principles of the dual inverter's voltage vector distribution are discussed in Section II(C), from where we know the voltage vector distribution point J (the common end of $\vec{u}_{s1}$ and $\vec{u}_{s2}$) has to be allocated inside the feasible region, which is the overlapping area of the two circles representing the voltage modulation ranges of the dual inverter. The MPSC algorithm makes the two circles overlap furthest by minimizing the amplitude of $\vec{u}_s$, which maximizes this feasible region.

Now we discuss how to allocate the voltage vector distribution point J. If we allocate J on $\vec{u}_s$, $\vec{u}_{s1}$ and $\vec{u}_{s2}$ will be colinear with $\vec{u}_s$, which is called the linear voltage vector distribution. This method can obtain the maximum available amplitude of $\vec{u}_s$. Please observe Fig.4 or Fig. 10, if we keep increasing the amplitude of $\vec{u}_s$, the feasible region of voltage vector distribution shrinks while the two circles gradually separate, and the angle range between $\vec{u}_{s1}$ and $\vec{u}_s$ shrinks at the same time. When the two circles are externally tangent, the linear voltage vector distribution is the only solution to synthesize $\vec{u}_s$. If the two circles separate completely, when $\vec{u}_s$

cannot be fully synthesized, the linear voltage vector distribution is the optimal choice under this circumstance.

However, the linear voltage vector distribution does not fully utilize power sharing potential of the feasible region. Taking inverter1 as an example, as shown in (11) we have $P_{inv1} = \vec{u_{s1}} \cdot \vec{i_s}$. The voltage modulation range without regard to the restriction of inverter2 is the circle centered at O_1 with a radius of $\sqrt{1/2}V_{dc1}$. Thus the maximum P_{inv1} takes place when $\vec{u_{s1}}$ with its maximum amplitude has the same direction with $\vec{i_s}$, and the minimum P_{inv1} takes place when $\vec{u_{s1}}$ has the opposite direction with $\vec{i_s}$, which are the points N_1 and $N_1^{'}$ shown in Fig. 10. However, N_1 and $N_1^{'}$ are not always inside the feasible region of the voltage vector distribution, such as the situation in Fig. 10. That is to say, if the linear voltage vector distribution could not satisfy the power sharing demand, and on the extended line of $\vec{i_s}$, points N_1 or $N_1^{'}$ are not inside the feasible region of the voltage vector distribution, the optimal $\vec{u_{s1}}$ should be found between the extended lines of $\vec{u_s}$ and $\vec{i_s}$. Therefore, we set the space angle of $\vec{u_{s1}}$ or $\vec{u_{s2}}$ in $\alpha\beta$ frame as the optimization variable, P_{inv1} as the optimization objective, and the extended lines of $\vec{u_s}$ and $\vec{i_s}$ as the searching boundary. The optimization goal is to find the optimal $\vec{u_{s1}}$ or $\vec{u_{s2}}$ inside the feasible region of the voltage vector distribution with the closest P_{inv1} to its expected value P^*_{inv1}.

As shown in Fig. 10, l_s is the extended line of $\vec{i_s}$ through point O_1, l_s' is the extended line of $-\vec{i_s}$ through point O_2. Taking inverter1 as an example, whether $\angle O_2O_1N_1$ or $\angle O_2O_1N_1'$ should serve as the searching range depends on the relation between the motor's input power P_m and inverter1's expected power P^*_{inv1}. If P_m and P^*_{inv1} have the same sign, the boundary on l_s should be along the direction of $\vec{i_s}$, otherwise it should be opposite to the direction of $\vec{i_s}$. In Fig. 10, the angle between $\vec{u_s}$ and $\vec{i_s}$ is obtuse, where $P_m = \vec{u_s} \cdot \vec{i_s}$ is minus, meaning the motor is in generating state. However, P^*_{inv1} is positive, thus the searching range of $\vec{u_{s1}}$ should be $\angle O_2O_1N_1$, marked as α_{GS}. Similarly, the searching range of $\vec{u_{s2}}$ should be $\angle O_1O_2P_2$, marked as α'_{GS}. Because the feasible region of the voltage vector distribution is a convex region, the extreme value of P_{inv1} must take place on the edge of the region, which consists of parts of the two circles. Therefore, the test points of the voltage vector distribution should only be sought on the edges of the voltage modulation ranges instead of inside them. In Fig. 10, $\overset{\frown}{M_1N_1'}$ arc marked in yellow is the set of the testing points of $\vec{u_{s1}}$, and arc $\overset{\frown}{M_2N_2'}$ is the set of the testing points of $\vec{u_{s2}}$.

B. THE GOLDEN SECTION SEARCH METHOD

The golden section (GS) search method is a classic one-dimensional search method. Compared to other optimization algorithms, the GS method has a lighter and more stable computational burden, and the number of iterations can be set flexibly, which is very suitable for the searching of voltage vector distribution, because the task requires an invariable and extremely short calculation period in the control chain of the OW-IM system.

Before the search starts, we need to assure the power sharing demand P^*_{inv1} cannot be satisfied at the searching boundary, otherwise the search is not necessary.

Along with the direction of $\vec{u_s}$, the output voltage vector of inverter1 $\vec{u_{s1\_u}}$ obtaining the exact P^*_{inv1} can be calculated as:

$$\vec{u_{s1\_u}} = P^*_{inv1}\,\vec{u_s}\,/P_m \tag{26}$$

The corresponding $\vec{u_{s2\_u}}$ can be obtained by (9) as $\vec{u_{s2\_u}} = \vec{u_{s1\_u}} - \vec{u_s}$. If we have $|\vec{u_{s1\_u}}| \le \sqrt{1/2}V_{dc1}$ and $|\vec{u_{s2\_u}}| \le \sqrt{1/2}V_{dc2}$, it means $\vec{u_{s1\_u}}$ is inside the feasible region of the voltage vector distribution.

On the other side of the searching boundary, along with the extended line of $\vec{i_s}$ from point O_1, the output voltage vector of inverter1 $\vec{u_{s1\_i}}$ obtaining the exact P^*_{inv1} can be calculated as:

$$\vec{u_{s1\_i}} = P^*_{inv1}\,\vec{i_s}\,/|\,\vec{i_s}\,|^2 \tag{27}$$

Similarly, along with the extended line of $-\vec{i_s}$ from point O_2, the output voltage vector of inverter2 $\vec{u_{s2\_i}}$ obtaining the exact P^*_{inv1} can be calculated as:

$$\vec{u_{s2\_i}} = (P^*_{inv1} - P_m)\,\vec{i_s}\,/|\,\vec{i_s}\,|^2 \tag{28}$$

Follow the same steps to judge whether $\vec{u_{s1\_i}}$ and $\vec{u_{s2\_i}}$ are inside the feasible region. If anyone of $\vec{u_{s1\_u}}$, $\vec{u_{s1\_i}}$ and $\vec{u_{s2\_i}}$ is valid, use it as the final solution of the voltage vector distribution, otherwise the golden section method should be executed.

During every iteration of the GS method, a new probe angle will be tested. The probe angle is a space angle in $\alpha\beta$ frame, in other words, the probe angle determines two parallel lines through O_1 and O_2 with the same space angle, representing the orientations of $\vec{u_{s1}}$ and $\vec{u_{s2}}$, respectively. Taking Fig. 10 as an example, the current probe angle is α_p, and the corresponding probe lines are l_t through O_1 and l_t' through O_2. As mentioned before, we should only focus on the edges of the voltage modulation ranges so that there are four test points of voltage vector distribution requiring attention, which are the intersections of line l_t and circle O_1, namely P_1 and Q_1, and the intersections of line l_t' and circle O_2, namely P_2 and Q_2. Using the method mentioned above, if we have $|\vec{u_{s1}}| \le \sqrt{1/2}V_{dc1}$ and $|\vec{u_{s2}}| \le \sqrt{1/2}V_{dc2}$, it means the current test point is valid (inside the feasible region of the voltage vector distribution). Then among all the valid points of the four test points, the point with the minimum power sharing deviation D_p will be selected as the solution of the current probe angle, where D_p is the deviation between inverter1's output power at the test point and its

expected value P^*_{inv1}. In Fig. 10, point P_1 will be selected as the solution of probe angle α_p among the two valid points P_1 and P_2.

It is worth mentioning that the voltage vector distribution is executed in the stationary $\alpha\beta$ frame, as shown in Fig. 2. Therefore, the voltage modulation ranges of the two inverters can be the two hexagons instead of the two inscribed circles. However, when giving the two parallel lines of the probe angle, it is much more complex to calculate the coordinates of the four test points when to use the two hexagons instead of the two circles, which will increase the computational burden of the algorithm. Thus, in above discussion we use two circles to illuminate, and it will cause a conservative result. It is practicable to use two hexagons for the calculation if only the processor is capable for the calculation. The method to acquire the intersections of a hexagon and a line through its center can be referred in [31].

After setting the number of iterations, the GS searching procedure can be executed, as shown in Fig. 11.

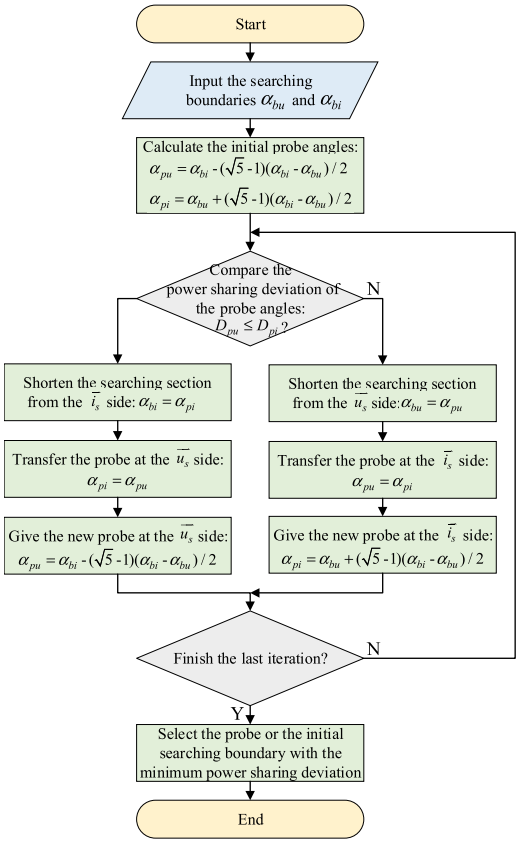

FIGURE 11. Flow chart of the golden section searching method.

In the flow chart, α_{bu} and α_{bi} are the searching boundary angles of the current iteration at the $\vec{u}_s$ side and the $\vec{i}_s$ side, respectively. For the first iteration, the searching boundary is set according to Section IV(A). α_{pu} and α_{pi} are the probe angles at the $\vec{u}_s$ side and the $\vec{i}_s$ side, D_{pu} and D_{pi} are the minimum power sharing deviations of probes α_{pu} and α_{pi}, respectively. After the specified number of iterations, the solution of the voltage vector distribution with a P_{inv1} closest to P^*_{inv1} can be acquired.

TABLE 2. Parameters of the hardware circuit and the controller.

Modules	Items	Parameters
solver	solver type	discrete
	time step T_s /s	5×10^{-7}
inverter devices	on-resistance R_{on} /Ω	0.0025
	forward voltage drop V_f /V	0.8
	current fall time and tailing time $[T_f, T_t]$/s	$[1.5,2]\times10^{-6}$
	current capacity of each phase $i_{\max}$ /A	260
power sources	DC-bus voltages of primary and secondary power source $[V_{dc1}, V_{dc2}]$/V	[350, 250]
motor speed controller	sampling time T_{s_SC} /s	1×10^{-4}
	proportionality coefficient P_{SC}	0.6
	integral coefficient I_{SC}	4
torque regulator	sampling time T_{s_TR} /s	1×10^{-4}
	lower limit of rotor flux $\psi^*_{r\_\min}$ /Wb	0.05
	maximum allowable change rate of rotor flux $R_{\max\_\psi r}$ /Wb·s^{-1}	20
current regulator (PID controller)	sampling time T_{s_CR} /s	1×10^{-4}
	proportionality coefficient P_{CR}	2
	integral coefficient I_{CR}	100
voltage vector distributor (GS)	sampling time T_{s_VD} /s	1×10^{-4}
	number of iterations n_i	3
SVPWM operator	sampling time T_{s_SVM} /s	1×10^{-4}
	switching cycle T_{c_SVM} /s	1×10^{-4}

V. SIMULATION VALIDATION OF THE OW-IM DRIVE SYSTEM

To validate the proposed strategies of the rotor flux calculation and the voltage vector distribution, we conduct a detailed simulation of the OW-IM drive system on the MATLAB/Simulink platform. The parameters of the motor are identical to Table 1. The hardware circuit and the controller parameters are set up according to Table 2. The expected output power of inverter1 P^*_{inv1} is set to 20 kW and holds constant. An additional motor speed controller using the PI control principle is introduced to generate the desired torque T^*_e to make the motor speed follow the preset value.

We also set a contrast model with the identical parameters. The only difference is that the contrast model uses the conventional flux inverse proportional control method: in the constant torque region the expected rotor flux amplitude ψ^*_r holds constant, and in the field weakening (FW) region ψ^*_r varies inversely proportional to the motor rotational speed.

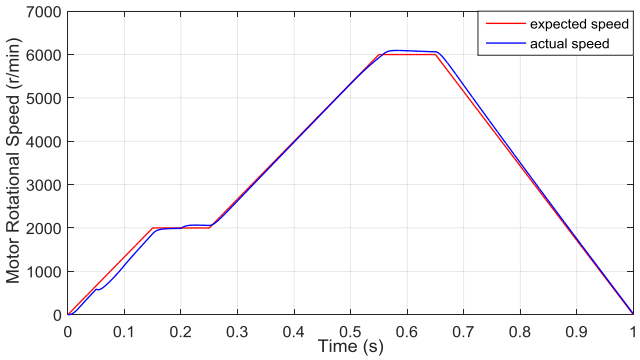

a) Expected and actual rotational speed

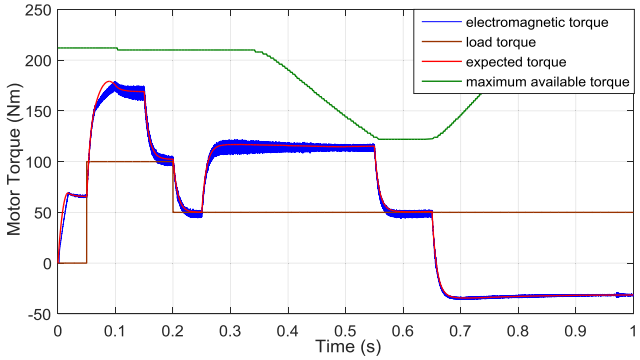

b) Electromagnetic torque, load torque, expected torque and maximum available torque

FIGURE 12. Curves of motor speed and torque.

The constant ψ_r^* is set to 0.2Wb, and the FW starting speed is set to 2500r/min.

The motor operation of total 1s is simulated. At the beginning, the expected motor speed linearly increases from 0 to 2000 r/min in 0–0.15 s and holds constant for 0.1 s. Then, it linearly increases to 6000 r/min in 0.3 s and holds constant for another 0.1s. Finally, the speed linearly drops to 0 in 0.35 s. The load torque steps from 0 to 100 Nm at 0.05 s and drops to 50 Nm at 0.2 s, then holds constant until the simulation finishes. Thus, the light-load and heavy-load conditions in the low-speed and high-speed regions, and the acceleration and deceleration processes of the drive system are all tested.

The expected and actual motor's rotational speeds are shown in Fig. 12(a); the electromagnetic torque, load torque, expected torque and maximum available torque are given in Fig. 12(b).

From the above figures we can observe that the motor speed can accurately follow the desired value. There are only two slight fluctuations at the saltation points of the load torque. Fig. 12(b) also shows that the electromagnetic torque can follow the desired value precisely in most time with the fluctuation lower than 15 Nm. After the motor starts to decelerate, the electromagnetic torque drops below zero to apply the braking torque. However, in the first 0.1 s, the electromagnetic torque cannot catch very well, because it requires a period building up the rotor flux with enough amplitude to support the electromagnetic torque after the motor started,

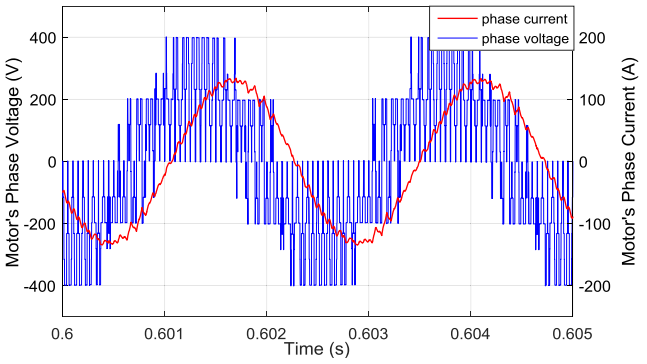

FIGURE 13. Partial waveforms of phase A's voltage and current.

which can also be observed from the curve of the rotor flux amplitude.

Partial waveforms of the single-phase voltage and current are shown in Fig. 13, sampled from 0.6-0.605 s of the motor's operation time.

In theory, the available voltage levels of the motor's phase voltage under the dual SVPWM scheme is increased from 5 to 9 compared to the single SVPWM scheme. Furthermore, there are more available phase voltage levels with the unequal DC-bus voltages of two power sources. We can observe that the waveform of the single-phase voltage is very close to the sine wave, hence the current ripple reduces significantly.

The curves of the rotor flux amplitude of the contrast model and the proposed strategy are shown in Fig. 14(a) and (b), respectively. The mode number of the torque regulator under the proposed flux regulation strategy is shown in Fig. 14(c).

From Fig. 14(a) we can see under the conventional flux regulation strategy, the expected rotor flux is only related with the motor speed. After the motor enters the field weakening region, the expected rotor flux decreases as the motor speed goes up. The actual rotor flux has a significant lag when the expected value changes due to the inductive inertia of the rotor. In the beginning, it takes about 0.1 s to build up the rotor flux. Thus, during this period the electromagnetic torque of the motor is confined.

In Fig. 14(c), the mode number 1, 2, 3 represent the activation of the MLM, MVVA, and MCVA algorithms, respectively. We can observe that during half of the operating time the MLM algorithm is selected to enhance the motor efficiency. But in the heavy-load and high-speed region, the MLM algorithm cannot satisfy the power sharing demand, therefore the MPSC algorithm is selected. For instance, after 0.65 s, the motor operates at the generating state, meaning that P_m is below zero, but P_{inv1}^* remains at 20kW, which is an extremely severe condition for the power sharing. Under this circumstance, the MCVA algorithm is selected to provide inverter1 the maximum output power. The corresponding expected and actual rotor flux amplitudes are shown in Fig. 14(b), from which we can see more variation than the conventional flux regulation strategy. The most obvious difference is that under the proposed strategy, the expected

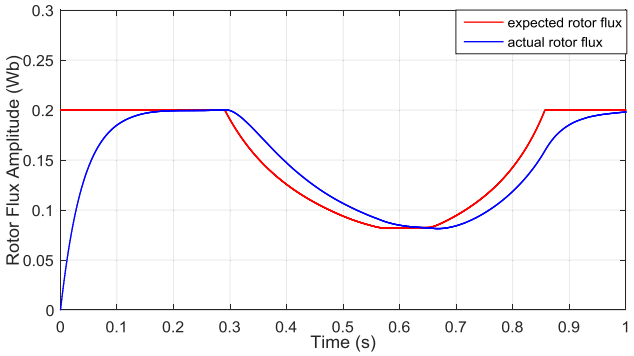

a) Expected and actual rotor flux amplitude of the contrast model

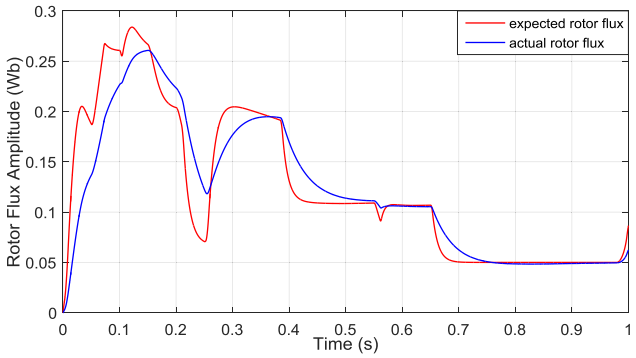

b) Expected and actual rotor flux amplitude of the proposed strategy

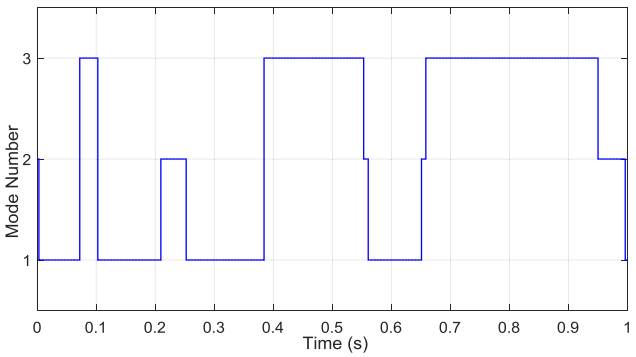

c) Mode number of the torque regulator

FIGURE 14. Curves of rotor flux amplitude.

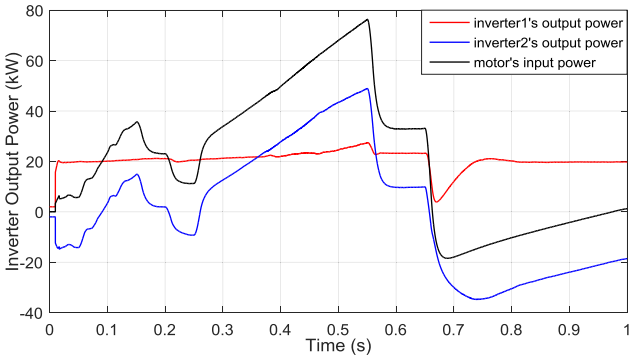

FIGURE 15. Output power of the two inverters under the proposed strategy.

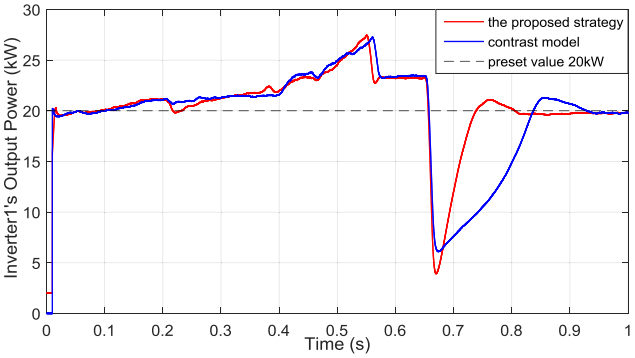

a) Comparison of different flux regulation strategies

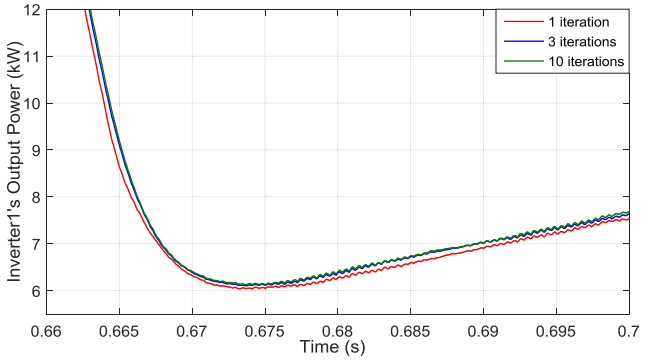

b) Comparison of different iteration number

FIGURE 16. Curves of inverter1's output power of different models.

rotor flux is related to not only the motor speed but also the desired torque. When the motor requires more torque, the expected rotor flux will increase as well. When the flux regulation algorithm shifts, such as 0.25 s and 0.65 s, a rapid change of the expected rotor flux occurs, which may lead to a major lag of the actual rotor flux due to its inductive inertia.

The output power of the two inverters and the input power of the motor under the proposed strategy are shown in Fig. 15.

The motor's input power P_m is determined by its output power and the efficiency. As shown in Fig. 15, it is shared by the output power of the two inverters. While inverter1 is set to follow P^*_{inv1} at 20kW, inverter2 is compensating the power notch or absorbing the excess power. After 0.65 s, when P^*_{inv1} is greater than P_m, P_{inv2} goes below zero, inverter2 is absorbing power outputted by both the motor and inverter1. In other words, the motor in generating state is charging power source2, at the same time power source1 is also charging power source2 through the motor.

The curves of inverter1's output power of different models are shown in Fig. 16. Fig. 16(a) gives the comparison between the proposed flux regulation strategy and the conventional flux inverse proportional control. Fig. 16(b) gives the comparison among different iteration numbers of the GS search in the voltage vector distribution.

From Fig. 16(a) we can observe, while inverter1's expected power P^*_{inv1} is fixed at 20 kW, inverter1's output power P_{inv1} can stay close to P^*_{inv1} under most circumstances as expected.

However, in some cases P_{inv1} cannot follow well. During 0.5-0.55 s, P_{inv1} gradually rolls up to 27 kW. At that time, the motor is in a rapid acceleration so that the electromagnetic torque and the amplitude of $\vec{i_s}$ are relatively high. Along with the high back electromotive force (EMF) caused by the high speed, the motor's stator voltage vector $\vec{u_s}$ goes nearly saturated. Thus, the power-sharing range is severely limited due to the shrinking feasible region of the voltage vector distribution, and inverter1 is forced to output a higher power to meet the demand of the motor. At 0.65 s, the motor starts deceleration, while the electromagnetic torque drops below zero to apply the braking torque. At that moment P_m drops to -20kW and P_{inv1} drops to 5kW rapidly, as shown in Fig. 15. As the motor speed goes down, P_m gradually increases again and P_{inv1} is getting back to 20kW. During most of the operating time, P_{inv1} under the proposed flux regulation strategy is following better than the conventional flux inverse proportional control, especially in 0.7-0.8 s during the deceleration of the motor, presenting advantages of the proposed MPSC algorithm. It is worth mentioning that at 0.55s and 0.65s, inverter1's power deviation under the proposed strategy is abnormally greater than the contrast model, which is caused by the saltation of the expected rotor flux amplitude when the flux regulation algorithm shifts. At that time actual rotor flux cannot follow the expected value immediately due to the inductive inertia, which can be observed in Fig. 14(b).

In order to study the effect of changing the iteration number of the GS search in the voltage vector distribution, the model under the conventional flux inverse proportional control is simulated 3 times with the iteration number set to 1, 3, 10, respectively. The result is, in most circumstances the differences are tiny. Because in most circumstances the power sharing demand can be directly satisfied by the linear voltage vector distribution without the need to involve the GS search. Therefore, we choose the local curve at 0.66-0.7 s during the deceleration to make a contrast, as shown in Fig. 16(b). It can be observed that even we enlarge the figure, the curves lay very close to each other. And the gap between the curves of 1 and 3 iterations is greater than the gap between 3 and 10 iterations, which means there are limited effects by increasing the iteration number, and the degree of this effect improvement decreases as the iteration number increases. Therefore, it is suitable to set a relatively small iteration number to lighten the computational burden while maintaining an acceptable optimization accuracy.

The curves of the motor electrical loss of the proposed strategy and the contrast model are shown in Fig. 17.

The motor electrical loss includes the copper loss and the iron loss, which reflects the electromechanical conversion efficiency of the motor. From Fig. 17 we can observe that in most of the operation time the motor electrical loss under the proposed strategy is less than the conventional flux inverse proportional control. However, at around 0.3 s and after 0.7 s, the conventional control performs better for different reasons. At around 0.3 s, the flux calculation algorithm has just shifted from the MVVA to the MLM when the rotor flux cannot follow rapidly due to the inductive inertia. After 0.7 s, the MPSC algorithm is activated to obtain a better power sharing capacity, thus the motor efficiency is set less of a priority.

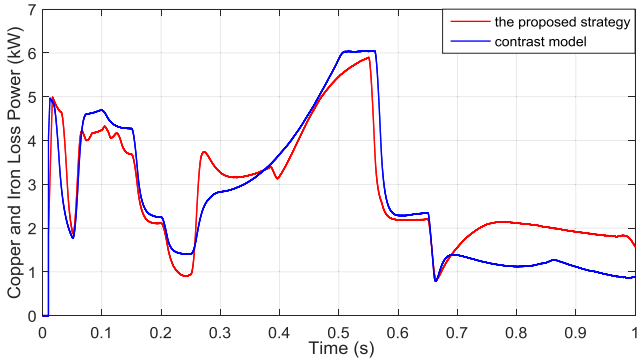

FIGURE 17. Curves of motor electrical loss.

VI. CONCLUSION

The OW-IM fed by dual inverter with two isolated power sources is studied in this paper. Two rotor flux calculation algorithms are proposed, which are the MLM algorithm and the MPSC algorithm. The MLM algorithm has the optimal efficiency performance, while the MPSC algorithm can maximize the power sharing capability of the dual inverter while holding the widest operation range of the motor. The algorithm selection strategy can pick the suitable rotor flux reference depending on the operating condition. Based on the dual SVPWM control scheme, the voltage vector distribution strategy involving the GS method fully utilizes the power sharing capability with a stable and efficient computational performance. Simulation results prove the validity of the proposed strategy, and show the potential in the energy management function for dual-power EVs.

However, there is also some room for improvement. At the present stage when the flux regulation algorithm shifts among the 3 algorithms, a saltation of the expected rotor flux often occurs, which may lead to a performance deterioration during the lag of the actual rotor flux due to its inductive inertia, especially when the operating conditions are changing drastically. Besides, the flux regulation and the voltage vector distribution are highly dependent on the accuracy of the motor parameters and state variables, which may cause the loss of control precision under severe conditions such as the drastic change in temperature. Thus, a high-precision parameter identification algorithm is needed to put this system into practical use.

Future research will be directed towards the above existing problems. And a test bench of the drive system will be built to validate the proposed scheme.

REFERENCES

[1] G. Nobile, G. Scelba, M. Cacciato, and G. Scarcellaet, "Losses minimization control for an integrated multi-drives topology devoted to hybrid electric vehicles," in *Proc. 43rd Annu. Conf. IEEE Ind. Electron. Soc. (IECON)*, Beijing, China, 2017.

[2] X. Sun, Z. Shi, G. Lei, Y. Guo, and J. Zhu, "Analysis and design optimization of a permanent magnet synchronous motor for a campus patrol electric vehicle," *IEEE Trans. Veh. Technol.*, vol. 68, no. 11, pp. 10535–10544, Nov. 2019.

[3] N. Xu, Y. Kong, L. Chu, H. Ju, Z. Yang, Z. Xu, and Z. Xu, "Towards a smarter energy management system for hybrid vehicles: A comprehensive review of control strategies," *Appl. Sci.*, vol. 9, no. 10, p. 2026, May 2019.

[4] M. J. Akhtar and R. K. Behera, "Optimal design of stator and rotor slot of induction motor for electric vehicle applications," *IET Electr. Syst. Transp.*, vol. 9, no. 1, pp. 35–43, Mar. 2019.

[5] X. Sun, K. Diao, G. Lei, Y. Guo, and J. Zhu, "Study on segmented-rotor switched reluctance motors with different rotor pole numbers for BSG system of hybrid electric vehicles," *IEEE Trans. Veh. Technol.*, vol. 68, no. 6, pp. 5537–5547, Jun. 2019.

[6] X. Sun, K. Diao, Z. Yang, G. Lei, Y. Guo, and J. Zhu, "Direct torque control based on a fast modeling method for a segmented-rotor switched reluctance motor in HEV application," *IEEE J. Emerg. Sel. Topics Power Electron.*, to be published, doi: 10.1109/jestpe.2019.2950085.

[7] X. Sun, K. Diao, G. Lei, Y. Guo, and J. Zhu, "Real-time HIL emulation for a segmented-rotor switched reluctance motor using a new magnetic equivalent circuit," *IEEE Trans. Power Electron.*, to be published, doi: 10.1109/tpel.2019.2933664.

[8] M. Zeraoulia, M. E. H. Benbouzid, and D. Diallo, "Electric motor drive selection issues for HEV propulsion systems: A comparative study," *IEEE Trans. Veh. Technol.*, vol. 55, no. 6, pp. 1756–1764, Nov. 2006.

[9] B. Sun, S. Gao, C. Ma, and J. Li, "System power loss optimization of electric vehicle driven by front and rear induction motors," *Int. J Autom. Technol.*, vol. 19, no. 1, pp. 121–134, Feb. 2018.

[10] X. Sun, J. Cao, G. Lei, Y. Guo, and J. Zhu, "Speed sensorless control for permanent magnet synchronous motors based on finite position set," *IEEE Trans. Ind. Electron.*, to be published, doi: 10.1109/tie.2019.2947875.

[11] X. Sun, L. Chen, Z. Yang, and H. Zhu, "Speed-sensorless vector control of a bearingless induction motor with artificial neural network inverse speed observer," *IEEE/ASME Trans. Mechatronics*, vol. 18, no. 4, pp. 1357–1366, Aug. 2013.

[12] C. Chih-Ming and Y. Kuang-Shine, "System integration and power flow management for the engine-generator operation of a range-extended electric vehicle," in *Proc. World Electr. Vehicle Symp. Exhib. (EVS)*, Barcelona, Spain, Nov. 2013.

[13] M. Camara, H. Gualous, F. Gustin, A. Berthon, and B. Dakyo, "DC/DC converter design for supercapacitor and battery power management in hybrid vehicle applications—Polynomial control strategy," *IEEE Trans. Ind. Electron.*, vol. 57, no. 2, pp. 587–597, Feb. 2010.

[14] C.-M. Lai, Y.-H. Cheng, M.-H. Hsieh, and Y.-C. Lin, "Development of a bidirectional DC/DC converter with dual-battery energy storage for hybrid electric vehicle system," *IEEE Trans. Veh. Technol.*, vol. 67, no. 2, pp. 1036–1052, Feb. 2018.

[15] S. Chowdhury, P. W. Wheeler, C. Patel, and C. Gerada, "A multilevel converter with a floating bridge for open-end winding motor drive applications," *IEEE Trans. Ind. Electron.*, vol. 63, no. 9, pp. 5366–5375, Sep. 2016.

[16] K. R. Sekhar and S. Srinivas, "Torque ripple reduction PWMs for a single DC source powered dual-inverter fed open-end winding induction motor drive," *IET Power Electron.*, vol. 11, no. 1, pp. 43–51, Jan. 2018.

[17] M. Jofre, A. M. Llor, and C. A. Silva, "Sensorless low switching frequency explicit model predictive control of induction machines fed by neutral point clamped inverter," *IEEE Trans. Ind. Electron.*, vol. 66, no. 12, pp. 9122–9128, Dec. 2019.

[18] S. Belkhode and S. Jain, "Optimized switching PWM technique with common-mode current minimization for five-phase open-end winding induction motor drives," *IEEE Trans. Power Electron.*, vol. 34, no. 9, pp. 8971–8980, Sep. 2019.

[19] S. Lakhimsetty and V. T. Somasekhar, "A four-level open-end winding induction motor drive with a nested rectifier-inverter combination with two DC power supplies," *IEEE Trans. Power Electron.*, vol. 34, no. 9, pp. 8894–8904, Sep. 2019.

[20] H. Machiya, H. Haga, and S. Kondo, "High efficiency drive method of an open-winding induction machine driven by dual inverter using capacitor across DC bus," *Elect. Eng. Jpn.*, vol. 197, no. 4, pp. 62–72, Dec. 2016.

[21] L. Harnefors, K. Pietilainen, and L. Gertmar, "Torque-maximizing field-weakening control: Design, analysis, and parameter selection," *IEEE Trans. Ind. Electron.*, vol. 48, no. 1, pp. 161–168, Feb. 2001.

[22] S.-H. Kim, S.-K. Sul, and M.-H. Park, "Maximum torque control of an induction machine in the field weakening region," in *Proc. IEEE Ind. Appl. Soc. Meeting*, Toronto, ON, Canada, Oct. 1993.

[23] S.-H. Kim and S.-K. Sul, "Voltage control strategy for maximum torque operation of an induction machine in the field-weakening region," *IEEE Trans. Ind. Electron.*, vol. 44, no. 4, pp. 512–518, Aug. 1997.

[24] R. Abdelati and M. F. Mimouni, "Optimal control strategy of an induction motor for loss minimization using Pontryaguin principle," *Eur. J. Control*, vol. 49, pp. 94–106, Sep. 2019.

[25] I. J. Smith and J. Salmon, "High-efficiency operation of an open-ended winding induction motor using constant power factor control," *IEEE Trans. Power Electron.*, vol. 33, no. 12, pp. 10663–10672, Dec. 2018.

[26] M. Chen and D. Sun, "A unified space vector pulse width modulation for dual two-level inverter system," *IEEE Trans. Power Electron.*, vol. 32, no. 2, pp. 889–893, Feb. 2017.

[27] Y. Ohto, T. Noguchi, and T. Sasaya, "Space vector modulation of dual inverter with battery and capacitor across DC buses," in *Proc. IEEE 12th Int. Conf. Power Electron. Drive Syst. (PEDS)*, Honolulu, HI, USA, Dec. 2017, pp. 1172–1177.

[28] A. K. Yadav, K. Gopakumar, K. R. R. L. Umanand, K. Matsuse, and H. Kubota, "Instantaneous balancing of neutral-point voltages for stacked DC-link capacitors of a multilevel inverter for dual-inverter-fed induction motor drives," *IEEE Trans. Power Electron.*, vol. 34, no. 3, pp. 2505–2514, Mar. 2019.

[29] A. Kumar, B. Fernandes, and K. Chatterjee, "DTC of open-end winding induction motor drive using space vector modulation with reduced switching frequency," in *Proc. IEEE 35th Annu. Power Electron. Spec. Conf.*, Aachen, Germany, vol. 2, Nov. 2004, pp. 1214–1219.

[30] V. Somasekhar, S. Srinivas, and K. Gopakkumar, "A space vector based PWM switching scheme for the reduction of common-mode voltages for a dual inverter fed open-end winding induction motor drive," in *Proc. IEEE 36th Conf. Power Electron. Spec.*, Oct. 2006, pp. 816–821.

[31] K. M. R. Eswar, K. V. P. Kumar, and T. V. Kumar, "A simplified predictive torque control scheme for open-end winding induction motor drive," *IEEE J. Emerg. Sel. Topics Power Electron.*, vol. 7, no. 2, pp. 1162–1172, Jun. 2019.

[32] D. Casadei, G. Grandi, A. Lega, and C. Rossi, "Multilevel operation and input power balancing for a dual two-level inverter with insulated DC sources," *IEEE Trans. Ind. Appl.*, vol. 44, no. 6, pp. 1815–1824, Nov. 2008.

[33] L. Chu, Y.-F. Jia, D.-S. Chen, N. Xu, Y.-W. Wang, X. Tang, and Z. Xu, "Research on control strategies of an open-end winding permanent magnet synchronous driving motor (OW-PMSM)-equipped dual inverter with a switchable winding mode for electric vehicles," *Energies*, vol. 10, no. 5, p. 616, May 2017.

[34] B. A. Welchko, "A double-ended inverter system for the combined propulsion and energy management functions in hybrid vehicles with energy storage," in *Proc. 31st Annu. Conf. IEEE Ind. Electron. Soc. (IECON)*, Raleigh, NC, USA, Nov. 2005, p. 6.

[35] A. Amerise, M. Mengoni, L. Zarri, A. Tani, S. Rubino, and R. Bojoi, "Open-end windings induction motor drive with floating capacitor bridge at variable DC-link voltage," *IEEE Trans. Ind. Appl.*, vol. 55, no. 3, pp. 2741–2749, May 2019.

[36] Y.-F. Jia, N. Xu, L. Chu, L.-F. Zhang, D. Zhao, Y.-K. Li, and Z.-H. Yang, "Power flow control strategy based on the voltage vector distribution for a dual power electric vehicle with an open-end winding motor drive system," *IEEE Access*, vol. 6, pp. 54910–54926, 2018.

YI-FAN JIA was born in 1992. He received the B.S. degree in automotive engineering from Jilin University, Changchun, China, in 2014, where he is currently pursuing the Ph.D. degree.

His research interests include drive technology of hybrid electric vehicle, and control of permanent magnet synchronous motor drive system for automotive applications.

NAN XU received the B.S., M.S., and Ph.D. degrees from Jilin University. He is currently an Associate Professor with the College of Automotive Engineering, Jilin University.

His researches focus on vehicle global optimization energy management, driver-vehicle-road system data mining and analysis, vehicle powertrain control strategies and evaluation, intelligent urban transportation system planning, and evaluation and motor design and control.

LIANG CHU received the B.S., M.S., and Ph.D. degrees from Jilin University. He is currently the Professor with the College of Automotive Engineering, Jilin University.

His researches focus on the key technology about electric vehicles and hybrid vehicles, vehicle dynamic, vehicle braking system control and design, and regenerative braking system control and design.

YUANJIAN ZHANG (Member, IEEE) received the M.S. degree in automotive engineering from Coventry University, U.K., in 2013, and the Ph.D. degree in automotive engineering from Jilin University, China, in 2018. In 2018, he joined the University of Surrey, Guildford, U.K., as a Research Fellow in advanced vehicle control.

He currently works with the Sir William Wright Technology Centre, Queen's University Belfast, U.K. His current research interests include advanced control on electric vehicle powertrains, vehicle-environment-driver cooperative control, vehicle dynamic control, and intelligent control for driving assist systems.

ZHE XU received B.S. and M.S. degrees from Jilin University. He is currently a Vehicle Designer with the FAW Research and Development Institute, China FAW Group Corporation.

His researches focus on the NVH control and structure design for powertrain mounting on internal combustion engine, electrical motor, and hybrid vehicles.

YU-KUAN LI was born in 1983. He received the B.S. and M.S. degrees in automotive engineering from the Changchun University of Technology, China. He is currently pursuing the Ph.D. degree with Jilin University.

His research interests include drive technology of hybrid electric vehicle and control of permanent magnet synchronous motor drive system for automotive applications.

ZHI-HUA YANG received the B.S. and M.S. degrees from the Jilin University of Technology. He is currently an Associate Professor with the College of Automotive Engineering, Jilin University. His researches focus on the key technology about powertrain for electric vehicles and vehicle testing.